Structural mechanism of transcription inhibition by lasso peptides microcin J25 and capistruin

Nathaniel R. Braffman[a,1], Frank J. Piscotta[b], Jesse Hauver[a], Elizabeth A. Campbell[a], A. James Link[b,c,d], and Seth A. Darst[a,2]

[a]Laboratory of Molecular Biophysics, The Rockefeller University, New York, NY 10065; [b]Department of Chemical and Biological Engineering, Princeton University, Princeton, NJ 08544; [c]Department of Chemistry, Princeton University, Princeton, NJ 08544; and [d]Department of Molecular Biology, Princeton University, Princeton, NJ 08544

Edited by James M. Berger, Johns Hopkins Medical Institute, Baltimore, MD, and approved December 13, 2018 (received for review October 9, 2018)

We report crystal structures of the antibacterial lasso peptides microcin J25 (MccJ25) and capistruin (Cap) bound to their natural enzymatic target, the bacterial RNA polymerase (RNAP). Both peptides bind within the RNAP secondary channel, through which NTP substrates enter the RNAP active site, and sterically block trigger-loop folding, which is essential for efficient catalysis by the RNAP. MccJ25 binds deep within the secondary channel in a manner expected to interfere with NTP substrate binding, explaining the partial competitive mechanism of inhibition with respect to NTPs found previously [Mukhopadhyay J, Sineva E, Knight J, Levy RM, Ebright RH (2004) *Mol Cell* 14:739–751]. The Cap binding determinant on RNAP overlaps, but is not identical to, that of MccJ25. Cap binds further from the RNAP active site and does not sterically interfere with NTP binding, and we show that Cap inhibition is partially noncompetitive with respect to NTPs. This work lays the groundwork for structure determination of other lasso peptides that target the bacterial RNAP and provides a structural foundation to guide lasso peptide antimicrobial engineering approaches.

capistruin | lasso peptide | microcin J25 | RNA polymerase | X-ray crystallography

Lasso peptides belong to a large superfamily of natural products derived from ribosomally synthesized polypeptide precursors (RiPPs) (1, 2) for ribosomally synthesized and posttranslationally modified peptides (3). Lasso peptides are posttranslationally modified by two enzymatic transformations into a right-handed, threaded 3D structure reminiscent of a slipknot or lasso. The mature peptide contains an isopeptide bond that joins the N terminus to a Glu or Asp side chain seven to nine residues toward the C terminus, forming an internal lactam ring. The remaining C-terminal portion of the peptide is threaded through the ring, giving rise to the lasso structure. In class II lasso peptides (2), the C-terminal tail is held in place noncovalently by steric locks, bulky amino acids that sterically prevent the tail from threading out of the ring (4–6). Two class II lasso peptides that have been identified as antimicrobial agents that target the bacterial RNA polymerase (RNAP) are microcin J25 (MccJ25) (7, 8) and capistruin (Cap) (9).

MccJ25 is secreted by strains of *Escherichia coli* (*Eco*) harboring a plasmid-borne synthesis, maturation, and export system (10, 11). MccJ25 was shown to have antimicrobial properties against a range of Gram-negative enterobacteria (10) through its ability to inhibit the bacterial RNAP (7, 8). The "threaded lasso" structure of MccJ25 was determined simultaneously by three groups (4–6). The determinant for MccJ25 binding to *Eco* RNAP has been well established to be the secondary channel through which NTP substrates reach the RNAP catalytic center (12, 13).

Genome mining was used to identify homologs of the MccJ25-processing enzymes in the *Burkholderia thailandensis* E264 (*Bth*) genome as well as a putative lasso peptide precursor (14). The predicted lasso peptide, Cap, was isolated from culture supernatants and shown to have antibacterial activity against related *Burkholderia* and *Pseudomonas* strains (14). Cap was shown to inhibit *Eco* RNAP in vitro but not a mutant *Eco*RNAP[β'^{T931I}] resistant to MccJ25 (7), suggesting that MccJ25 and Cap share the RNAP secondary channel as their binding determinant (9).

Here we determine crystal structures of MccJ25 and Cap bound to *Eco* RNAP. The structures define peptide–RNAP interactions that are important for inhibition and provide detailed insight into the peptides' inhibition mechanisms that are corroborated by biochemical assays. This work lays the groundwork for the determination of structures of other lasso peptides that target the bacterial RNAP (15) and provides a structural foundation to guide lasso peptide antimicrobial engineering approaches (16, 17).

Results

Previously, we and several other groups determined crystal structures of *Eco* RNAP holoenzyme (the catalytic core RNAP, E, plus the promoter specificity σ^{70} subunit, i.e., Eσ^{70}) from the same $P2_12_12_1$ crystal form (18–20). With this crystal form, we could not obtain a complex with MccJ25 or Cap by soaking or cocrystallization. The key to obtaining MccJ25/Eσ^{70} and Cap/Eσ^{70} structures was the discovery of a new *Eco* Eσ^{70} crystal form.

A Crystal Form of *Eco* Eσ^{70} That Supports MccJ25 and Cap Binding. In the course of crystallization trials that included *Eco* Eσ^{70}, the transcription factor CueR (21), and an upstream-fork (us-fork) promoter fragment derived from the CueR-regulated *copA* promoter (*copA* us-fork−38; *SI Appendix*, Fig. S1*A*), we obtained crystals in space group $P4_12_12$ that diffracted X-rays to better than 4-Å resolution. The structure was determined by molecular

Significance

Many bacteria produce antimicrobial peptides for survival under stressful conditions. Some of these antimicrobial peptides are lasso peptides, which have a unique lasso-like topology and have generated great interest as a result of their stability in harsh conditions and amenability to functional engineering. In this study, we determined crystal structures of two lasso peptides, microcin J25 and capistruin, bound to their natural enzymatic target, the bacterial RNA polymerase (RNAP). The structures define peptide inhibitor–RNAP interactions that are important for inhibition and provide detailed insight into how the peptides inhibit RNAP function. This work provides a structural basis to guide the design of more potent lasso peptide antimicrobial approaches.

Author contributions: E.A.C., A.J.L., and S.A.D. designed research; N.R.B., F.J.P., J.H., and S.A.D. performed research; N.R.B., F.J.P., J.H., E.A.C., and S.A.D. analyzed data; and E.A.C., A.J.L., and S.A.D. wrote the paper.

The authors declare no conflict of interest.

This article is a PNAS Direct Submission.

Data deposition: The atomic coordinates and structure factors have been deposited in the Protein Data Bank, www.wwpdb.org (PDB ID codes 6N60, 6N61, and 6N62).

[1]Present address: Department of Chemistry & Chemical Biology, Harvard University, Cambridge, MA 02138.

[2]To whom correspondence should be addressed. Email: darst@rockefeller.edu.

This article contains supporting information online at www.pnas.org/lookup/suppl/doi:10.1073/pnas.1817352116/-/DCSupplemental.

Published online January 9, 2019.

replacement (19), revealing that Eσ^{70} bound to the promoter DNA fragment in an unusual manner and without CueR. The same crystals were obtained in subsequent crystallization trials without the addition of CueR. In these crystals, the −10 element of the us-fork promoter DNA fragment was engaged with σ$^{70}_2$, as seen in other RNAP-holoenzyme structures with us-fork promoter fragments (22–24), but the −35 element of the promoter DNA fragment was not bound to σ$^{70}_4$ as expected; instead, the duplex DNA upstream of the −10 element veered away from σ$^{70}_4$ and was bound in the downstream duplex DNA channel of a symmetry-related Eσ^{70} complex (*SI Appendix*, Fig. S1*B*). Examination of the electron density and modeling of the upstream DNA suggested that truncating the DNA from the upstream end might improve the crystals, and indeed more reproducible and better diffracting crystals were obtained by using the us-fork promoter fragment *copA* us-fork−35 (*SI Appendix*, Fig. S1*A*). Diffraction data were collected, and a model was built and refined to 3.8-Å resolution (*SI Appendix*, Fig. S1*B* and Table S1). This crystal form supported binding of both MccJ25 and Cap (Figs. 1 and 2).

An MccJ25/Eσ^{70} Crystal Structure. Mature MccJ25 is a 21-aa residue class II lasso peptide with an isopeptide bond between the N terminus (G1) and the side chain of E8, forming an 8-residue ring (4–6). The C-terminal tail threads through the ring, with steric lock residues F19 and Y20 on opposite sides of the ring (Fig. 1*A*). The structure and activity of MccJ25 is stable to harsh denaturing conditions (6), indicating that the steric lock residues are unable to pass through the ring, thereby maintaining the threaded MccJ25 structure without covalent attachment.

To provide a structural basis for understanding MccJ25 inhibition of *Eco* RNAP, we incubated the $P4_12_12$ us-fork/Eσ^{70} crystals with 100 μM MccJ25 and determined the crystal structure to 3.7-Å resolution (Fig. 1 and *SI Appendix*, Table S1). Unbiased Fourier difference maps revealed unambiguous electron density defining the location of MccJ25 binding in the RNAP secondary channel as expected, but the low resolution of the maps made determination of the peptide orientation ambiguous.

To confirm the binding orientation of MccJ25, we used the amber suppression approach to generate MccJ25 derivatives containing *para*-Bromo-Phe substituted at H5 (MccJ25[H5*p*BrF]) or F10 (MccJ25[F10*p*BrF]) (25) (*SI Appendix*). Fourier difference maps indicated binding of the MccJ25 derivatives. Anomalous difference Fourier maps revealed single Br peaks for each derivative (Fig. 1*B*). The resulting localization of MccJ25 H5 and F10 allowed the unambiguous placement and refinement of an MccJ25 atomic model into the density (Fig. 1*C* and *SI Appendix*, Table S1). The entire MccJ25 molecule was modeled except for the side chain of F19, which was disordered. Comparing RNAP-bound MccJ25 with FhuA-bound [Protein Data Bank (PDB) ID code 4CU4] (26) and free MccJ25 (PDB ID code 1Q71) (5) reveals that the lactam ring and threaded tail portions of the peptide (residues 1–8 and 19–21) are relatively rigid (rmsd values of 1.5 and 1.3 Å over 11 α-carbons, respectively), whereas the loop region (residues 9–18) shows extensive deviations among all three structures (rmsd values of 5.5 and 7.8 Å, respectively; *SI Appendix*, Fig. S2*A*).

MccJ25–RNAP Interactions. MccJ25 binds within the RNAP secondary channel (Fig. 1*C*), as predicted from previous studies (12, 13). The MccJ25 binding determinant on RNAP defined structurally (Fig. 1*C*) is consistent with the binding determinant defined through MccJ25 resistance mutations (*SI Appendix*, Fig. S2*B*) (8, 13). The peptide orients with the ring and tail proximal to, and with the loop distal to, the RNAP active site (Fig. 1). MccJ25 binds deep within the secondary channel, with the ring residue H5 located only 6.5 Å from the RNAP active site Mg^{2+}.

The binding of MccJ25 in the RNAP secondary channel buries a surface area of 960 Å^2 (27). The peptide interacts with RNAP structural elements within the secondary channel and near the active site (28), including the β′ subunit F-loop (29), bridge helix (BH), residues of the unfolded TL, the shelf, as well as residues of the β-subunit near the active site (Fig. 1 *D* and *E*).

MccJ25-Y9 was found to be strictly essential for RNAP inhibition (30), and this residue makes the most extensive interactions with RNAP (Fig. 1 *D* and *E*). More than 80% of the MccJ25-Y9–accessible surface area is buried in interactions with the F-loop (β′R744, M747), the BH (β′S775, G778, A779), and β-residues D675 and N677. In addition, the MccJ25-Y9 side chain-OH group acts as a hydrogen bond (H-bond) donor (with βD675, 3.2 Å) and H-bond acceptor (with β′R744, 3.2 Å). The critical importance of Y9 to MccJ25 activity was also highlighted by our finding that MccJ25 Y9 substituted with BrF was severely defective at RNAP inhibition (*SI Appendix*, Fig. S2*C*).

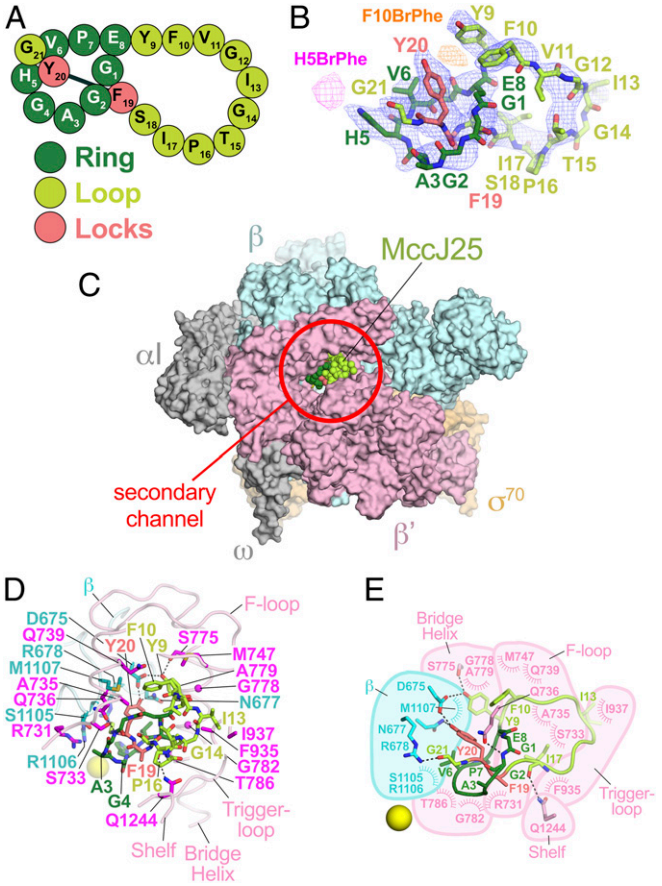

Fig. 1. Structure of MccJ25/Eσ^{70}. (*A*) Schematic illustration of lasso peptide MccJ25. (*B*) The atomic model for MccJ25 from the MccJ25/Eσ^{70} crystal structure is shown along with the 3.7-Å resolution $2F_o - F_c$ map (blue mesh, contoured at 1σ) and the Br anomalous Fourier difference peaks from crystals containing MccJ25[F10*p*BrF] (orange mesh, contoured at 5σ) or MccJ25[H5*p*BrF] (magenta mesh, contoured at 3σ). Carbon atoms of MccJ25 are colored according to *A*. The side chain for MccJ25-F19 was disordered and not modeled. (*C*) The overall structure of MccJ25/Eσ^{70} (DNA not shown for clarity; *SI Appendix*, Fig. S1) viewed into the secondary channel. Eσ^{70} is shown as a molecular surface with subunits colored as labeled. MccJ25 is shown as Corey–Pauling–Koltun (CPK) spheres and colored according to *A*. (*D*) MccJ25–RNAP interactions. RNAP structural elements that harbor residues interacting with MccJ25 are shown as backbone worms. Residues that interact with MccJ25 are shown in stick format. MccJ25 is shown in stick format with carbon atoms colored according to *A*. Polar interactions are denoted by dashed gray lines. The RNAP active-site Mg^{2+} is shown as a yellow sphere. (*E*) Schematic summary of MccJ25–RNAP interactions. MccJ25 is shown as a backbone worm with side chains of key residues shown. RNAP residues that make only nonpolar contacts are shown as labels with arcs denoting the contacts. The side chains of residues that make polar contacts are shown in stick format (polar contacts are denoted by dashed gray lines).

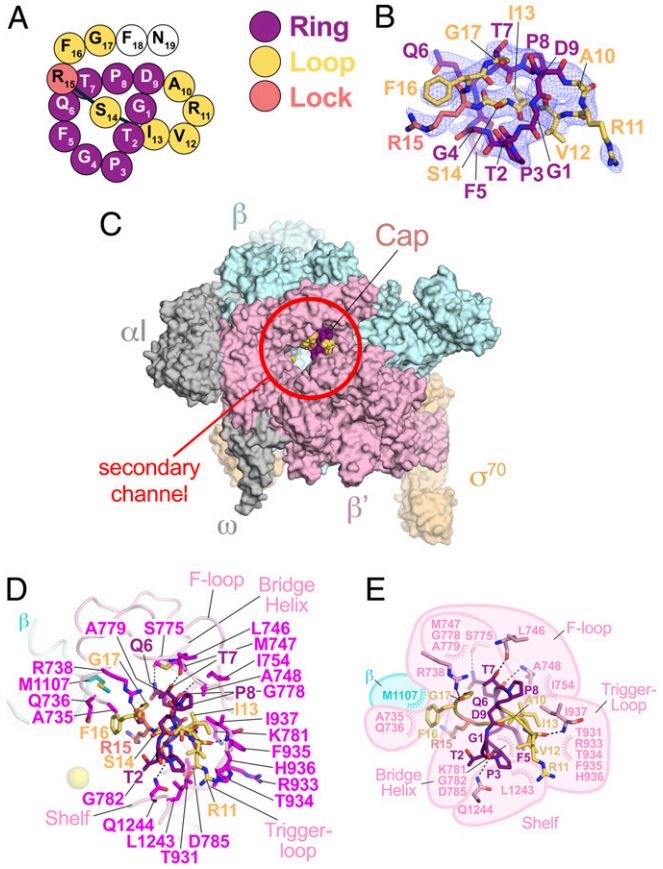

Fig. 2. Structure of Cap/Eσ^{70}. (*A*) Schematic illustration of lasso peptide Cap. Residues F18 and N19 were disordered in the crystal structure and are shown as open circles. (*B*) The atomic model for Cap from the Cap/Eσ^{70} crystal structure is shown along with the 3.25-Å resolution $2F_o - F_c$ map (blue mesh, contoured at 1.5σ). Carbon atoms of Cap are colored according to *A*. (*C*) The overall structure of Cap/Eσ^{70} (DNA is not shown for clarity; *SI Appendix*, Fig. S1) viewed into the secondary channel. Eσ^{70} is shown as a molecular surface with subunits colored as labeled. Cap is shown as CPK spheres and colored according to *A*. (*D*) View of Cap–RNAP interactions. RNAP structural elements that harbor residues interacting with Cap are shown as backbone worms. Residues that interact with Cap are shown in stick format. Cap is shown in stick format with carbon atoms colored according to *A*. Polar interactions are denoted by dashed gray lines. The RNAP active-site Mg^{2+} is shown as a yellow sphere. (*E*) Schematic summary of Cap/RNAP contacts. Cap is shown as a backbone worm with side chains of key residues shown. RNAP residues that make only nonpolar contacts are shown as labels with arcs denoting the contacts. The side chains of residues that make polar contacts are shown in stick format (polar contacts are denoted by dashed gray lines).

The C terminus of MccJ25 (G21) forms a salt bridge with the side chain of βR678 (2.5 Å; Fig. 1*E*). Amidation of the MccJ25 C terminus, which would disrupt this interaction, blocks RNAP inhibition (31).

The RNAP secondary channel is a narrow pore through which NTP substrates can access the RNAP active site when the RNAP active site cleft is occupied with nucleic acids (32, 33). The pore is approximately 15–20 Å in diameter but constricts near the RNAP active site to a diameter of less than 11 Å. The bound MccJ25 does not completely seal off the secondary channel but further constricts the solvent-accessible path to a gap of less than 5 Å (Fig. 1*C*). Although thermal motions of RNAP and MccJ25 could potentially expand this gap, in the presence of MccJ25, NTP substrates would have great difficulty reaching the RNAP active site through the secondary channel.

A Cap/Eσ^{70} Crystal Structure. Mature Cap is a 19-aa residue class II lasso peptide with an isopeptide bond between the N terminus (G1) and the side chain of D9, forming a 9-residue ring (14). The C-terminal tail threads through the ring, with steric lock residue R15 maintaining the threaded Cap structure without covalent attachment (Fig. 2*A*). To provide a structural basis for understanding Cap inhibition of *Eco* RNAP, we incubated the $P4_12_12$ us-fork/Eσ^{70} crystals with 100 μM Cap and determined the crystal structure to 3.2-Å resolution (Fig. 2 and *SI Appendix*, Table S1). Unbiased Fourier difference maps revealed unambiguous electron density defining the location of Cap binding in the secondary channel as expected (9) and allowed the unambiguous placement and refinement of a Cap atomic model comprising residues 1–17 (Cap residues F18 and N19 were disordered) into the density (Fig. 2 *B* and *C* and *SI Appendix*, Table S1).

Cap–RNAP Interactions. Like MccJ25, Cap binds within the RNAP secondary channel (Fig. 2*C*), consistent with the finding that the RNAP *Eco* RNAP[β′^{T931I}] substitution is resistant to both MccJ25 and Cap (9). Cap is also oriented with its ring and tail proximal to, and with its loop distal to, the RNAP active site (Fig. 2). Although Cap interacts with the same RNAP structural elements as MccJ25 (β′ F-loop, BH, unfolded TL, shelf; β-residues near the RNAP active site; Fig. 2 *D* and *E*) and interacts with many of the same RNAP residues (*SI Appendix*, Table S2), the Cap and MccJ25 binding determinants are distinct. The Cap binding determinant on RNAP is shifted away from the RNAP active site compared with MccJ25; the closest approach of any Cap atom to the RNAP active site Mg^{2+} is 12 Å (side chain of Cap-R15), compared with 6.5 Å for MccJ25. The center of mass of Cap is 22.3 Å from the RNAP active site Mg^{2+}, compared with 17.9 Å for MccJ25. Because Cap binds further from the RNAP active site where the secondary channel is wider, its presence does not appear to restrict access of NTP substrates to the RNAP active site (Fig. 2*C*).

The binding of Cap in the RNAP secondary channel buries a surface area of 970 Å^2, essentially identical to MccJ25. This is consistent with findings that both lasso peptides inhibit *Eco* RNAP in in vitro transcription reactions with the same K_i of ~1 μM (9, 13).

MccJ25 and Cap Block TL Folding. The RNAP nucleotide addition cycle is controlled by alternate closure (i.e., folding) and opening (i.e., unfolding) of a mobile structural element of the β′ subunit called the trigger loop (TL). Translocation of the elongation complex (EC) along the DNA template, as well as entry and binding of the NTP substrate through the secondary channel into the active site, is facilitated by an open active site with an unfolded TL (34). Folding of the TL is stabilized by direct contacts with the correct NTP substrate, which closes the active site. TL contacts with the NTP then position the substrate into precise reactive alignment to accelerate the polymerization reaction by ~10^4 (35–37). MccJ25 and Cap, when bound to RNAP, introduce severe steric clash with the folded TL (Fig. 3). Thus, in the presence of MccJ25 or Cap, TL folding appears to be disallowed, explaining an important component of the inhibition mechanisms for both peptides.

MccJ25, but Not Cap, Clashes with NTP Substrate Binding. Mukhopadhyay et al. (13) found that high concentrations of NTP substrates could overcome MccJ25 inhibition. Quantitative analysis of the NTP concentration-dependence of MccJ25 inhibition of *Eco* RNAP transcription activity showed that the mode of MccJ25 inhibition was partially competitive (13). In other words, MccJ25 binds to a site on RNAP that does not completely exclude NTP binding but increases the K_m for NTPs (38).

We modeled the position of the NTP substrate by superimposing the structure of a *Thermus thermophilus* RNAP de novo initiation complex (PDB ID code 4Q4Z) (39) onto the

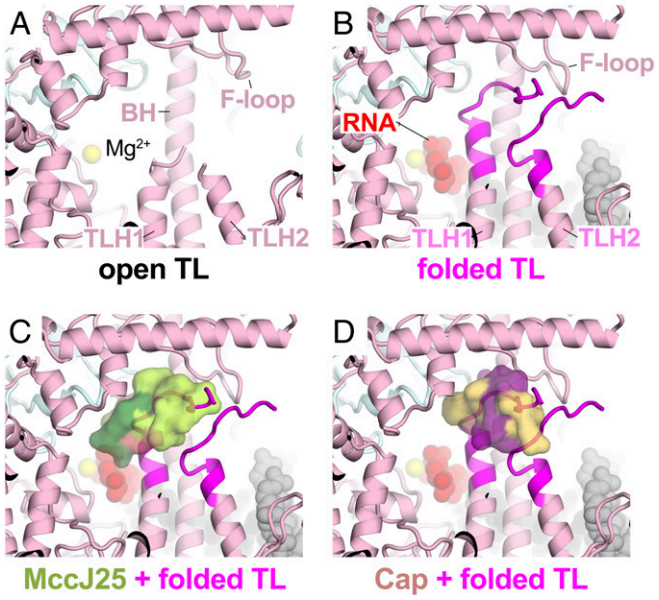

Fig. 3. MccJ25 and Cap sterically block RNAP TL folding. (*A–D*) Views of *Eco* RNAP structures into the secondary channel. The RNAP is shown as a backbone ribbon (β, light cyan; β′, light pink). The RNAP active-site Mg^{2+} is shown as a yellow sphere. (*A*) Structure of *Eco* RNAP with open (unfolded) TL (PDB ID code 4LJZ) (19). Except for the base helices (TLH1, TLH2), most of the TL is disordered. (*B*) Structure of *Eco* RNAP transcription initiation complex with a folded TL (PDB ID code 4YLN) (50). Newly ordered portion of the folded TL is colored magenta (β′i6 or SI3, a domain inserted into the middle of the *Eco RNAP* TL, is not shown for clarity) (51). Nucleic acids are shown as CPK spheres (DNA, gray; posttranslocated RNA transcript, red). (*C*) Same as *B* but with MccJ25 (shown as a molecular surface) superimposed. (*D*) Same as *B* but with Cap (shown as a molecular surface) superimposed.

MccJ25/Eσ^{70} structure (Fig. 4*A*), revealing steric clash between the triphosphate moiety of the 3′-NTP substrate and the side chain of MccJ25-H5 (Fig. 4*A*). Moreover, the negatively charged MccJ25 C terminus (G21) is positioned immediately adjacent to the negatively charged γ-phosphate.

Although the significant steric clash revealed by the modeling might suggest that MccJ25 could inhibit through a fully competitive mechanism (i.e., increasing the K_m for the NTP to infinity) (38), thermal molecular motions/flexibility must also be taken into account. Although the positioning of the NTP substrate would need to be precise for efficient catalysis, flexibility of the MccJ25 ring (where H5 is positioned) and C-terminal tail, as well as alternative rotamers for the side chain of MccJ25-H5, could allow NTP binding, accounting for the partial competitive inhibition mechanism.

Because Cap binds further away from the RNAP active site than MccJ25, the same modeling exercise shows that the NTP substrate and Cap are easily accommodated simultaneously (Fig. 4*B*). The closest approach between Cap and NTP atoms is 6.4 Å (side chain of Cap-R15 and an NTPγ-phosphate oxygen). This, combined with the finding that Cap binding does not appear to restrict NTP access to the RNAP active site (Fig. 2*C*), suggests that Cap inhibition would not exhibit NTP concentration dependence.

To test the structure-based hypothesis that Cap inhibition of RNAP transcription activity is not NTP concentration-dependent, we investigated RNAP transcription activity at each of four initiating substrate concentrations (12.5–100 μM UTP) and at four Cap concentrations (0–100 μM) by using a quantitative abortive initiation assay (*SI Appendix*, Fig. S2*D*). Quantitative analysis of the data indicates that the mode of inhibition by Cap is partially noncompetitive with respect to the NTP substrate (Fig. 4*C*). In other words, Cap and the NTP substrate can bind RNAP simultaneously without much effect on each other, but the Cap–NTP–RNAP complex has a reduced catalytic efficiency (by a factor of $\beta = 0.13$; Fig. 4*C*).

Discussion

Our results clarify the structural mechanisms for the inhibition of *Eco* RNAP by the lasso peptides MccJ25 and Cap. Consistent with previous results, both peptides bind in the RNAP secondary channel. In addition, both peptides bind in positions that prevent proper folding of the RNAP TL, which is required for efficient catalysis.

The MccJ25 and Cap binding determinants overlap with each other but are not identical (*SI Appendix*, Table S2). The MccJ25 and Cap binding determinants also overlap with but are not identical to binding determinants for the depsipeptide bacterial RNAP inhibitor salinamide A (SalA; ref. 40) and the eukaryotic RNAP II inhibitor α-amanitin (αAm; ref. 41). Like MccJ25 and Cap, SalA and αAm sterically interfere with RNAP TL folding. The MccJ25, Cap, SalA, and αAm binding determinants and inhibition mechanisms are distinct from those of other known RNAP inhibitors (*SI Appendix*, Fig. S3 and Table S3).

MccJ25 binds relatively deep within the secondary channel near the RNAP active site and would be expected to severely limit, or even prevent, NTP substrate access to the RNAP active site through the secondary channel (Fig. 4*A*). MccJ25 would be expected to limit all molecular traffic through the secondary channel into and out from the RNAP active site, and MccJ25 has been shown to inhibit RNAP backtracking, a process that involves threading of an ssRNA transcript 3′ segment out through the RNAP secondary channel (12). Furthermore, MccJ25 and NTP substrate binding are not structurally independent. Modeling with static structures indicates a steric clash that could potentially be relieved by flexibility in the MccJ25 molecule, explaining why MccJ25 inhibition of RNAP activity is partially competitive with respect to NTP binding (13).

By contrast, Cap binds further away from the RNAP active site, does not appear to restrict access of NTP substrates to the active site, and does not interfere with NTP substrate binding (Fig. 4*B*). Indeed, we find that Cap inhibition is partially noncompetitive with respect to NTP binding (Fig. 4*C*). According to our analysis, Cap and NTP substrate bind to RNAP simultaneously, but the rate of phosphodiester bond formation by the Cap/RNAP complex is approximately eightfold lower than that of RNAP. We presume Cap inhibition of RNAP catalysis is primarily through blocking of TL folding.

Proper folding and function of the TL, although not required for catalysis, enhances the rate of nucleotide addition ~10^4-fold in bacteria (35–37). This presents a paradox, as Cap-mediated inhibition of TL folding has only an approximately eightfold inhibitory effect. Residues of the folded TL, such as *Eco* β′H936, directly contact the phosphoryl groups of the NTP substrate, positioning the substrate for optimal catalysis through steric effects (42). RNAP structures containing the initiating substrate with a folded TL show that the residue corresponding to *Eco* β′ H936 is within 3.1 Å (PDB ID code 2O5J; ref. 35) and 3.4 Å (PDB ID code 2E2H; ref. 36) of the initiating NTP. Cap residues R15 and F16, although approaching the NTP (Fig. 4*B*), are too far away (≥6.4 Å) to play such a role. The bound Cap sterically interferes primarily with a loop at the top of TL-helix 1, not the folded position of the TL-helix itself (Fig. 3*D*). It is possible that partial TL folding can occur even in the presence of Cap, which could explain the discrepancy between the large effect of deleting the entire TL compared with the smaller effect of Cap binding.

RiPPs are an emerging class of natural products with vast structural diversity (3). Many RiPPs display potent antimicrobial activity and hold promise for therapeutic agents (43). The relatively large size of RiPPs can allow for inhibition of sites that may

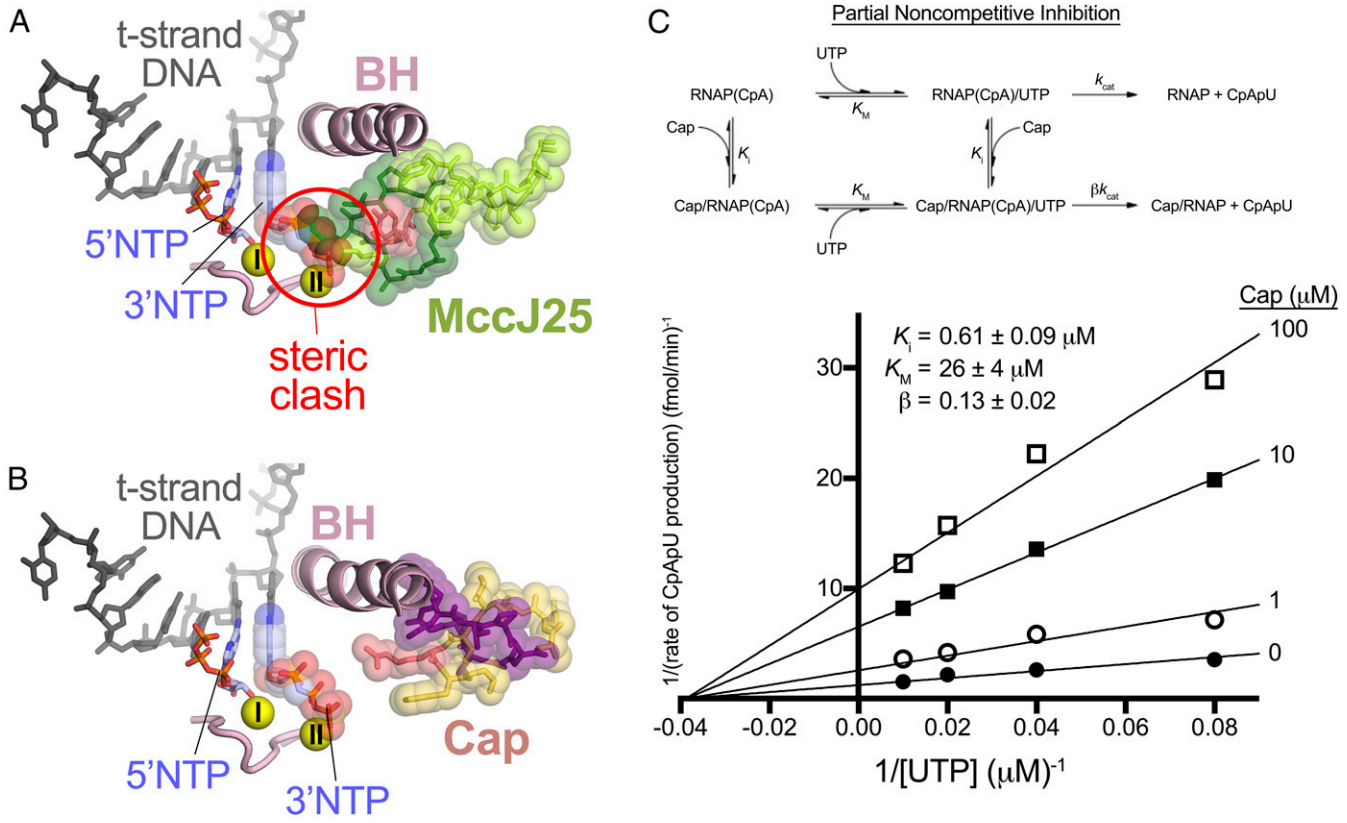

Fig. 4. McCJ25, but not Cap, clashes with NTP substrate binding. (*A*) View of the RNAP active site from the *T. thermophilus* de novo initiation complex (PDB ID code 4Q4Z) (39) with McCJ25 superimposed. Shown is the template-strand DNA from +1 to −5 (dark gray), the initiating NTP substrates (5′ and 3′; the 3′NTP is shown with transparent CPK spheres; note that the position of the 3′-NTP is identical to the position of the NTP substrate in an EC), and two Mg^{2+} ions (yellow spheres). McCJ25 is shown in stick format with transparent CPK spheres. The steric clash between the 3′NTP phosphate moieties and McCJ25 (mainly H5) is noted. (*B*) Same as *A* but with Cap superimposed. (*C*, *Top*) Partial noncompetitive model of inhibition that best fits the transcription assays (*SI Appendix*, Fig. S2*D*). RNAP(CpA) represents the RNAP open promoter complex prebound to initiating dinucleotide CpA. The assay measures the rate of production of CpApU from CpA and the substrate UTP at four UTP concentrations (12.5, 25, 50, and 100 μM) and its inhibition at four Cap concentrations (0, 1, 10, and 100 μM). The fitted parameters K_i, K_m, and β are shown within the context of the model. (*C*, *Bottom*) Double-reciprocal plot for inhibition of synthesis of CpApU by Cap. Lines are fit to a partial noncompetitive model of inhibition (*Top*); the values for the fitted parameters are shown (r^2 = 0.99). Within experimental error, the K_m for substrate UTP is independent of Cap concentration.

not be easily blocked by small molecules. Lasso peptides are a growing class of RiPPs that have attracted interest because of their unique structural characteristics, biological activities, remarkable stability (2, 6), and potential for engineering novel functions (16, 17). Here we determined molecular structures of two lasso peptides, McCJ25 and Cap, bound to their natural enzymatic target, the bacterial RNAP, providing insights into McCJ25 and Cap inhibition mechanisms. Additional class II lasso peptides from *Acinetobacter gyllenbergii* and *Klebsiella pneumoniae*, acinetodin and klebsidin, respectively, have been isolated and shown to inhibit *Eco* RNAP (15). Although not obviously related to McCJ25 or Cap, they both act by binding in the RNAP secondary channel. The approach used here to structurally characterize McCJ25 and Cap complexes with *Eco* RNAP should allow the structural characterization of acinetodin and klebsidin complexes with RNAP as well. Furthermore, these results provide a framework to guide the discovery of additional RNAP-targeting lasso peptides and to enable the engineering of lasso peptides for improved antimicrobial activity.

Materials and Methods

Protein Expression and Purification. *Eco* core RNAP lacking the αC-terminal domain (αCTD) was prepared as described previously (44). *Eco* full-length σ^{70} and $\Delta1.1\sigma^{70}$ were prepared as described previously (19).

Lasso Peptide Preparation. McCJ25 and Cap were produced in *Eco* by using refactored gene clusters described previously (45, 46). McCJ25 variants with BrPhe substitutions were generated in the same way by using orthogonal aminoacyl-tRNA synthetase–tRNA pairs to site-specifically insert the unnatural amino at the desired locations. Full details are provided in *SI Appendix*.

Crystallization. To prepare DNA (*SI Appendix*, Fig. S1*A*), lyophilized oligonucleotides (Oligos Etc) were dissolved in 20 mM Tris·HCl, pH 8.0, 0.5 mM EDTA, 0.2 M NaCl to 2 mM. Equimolar amounts of the complementary oligonucleotides were annealed by heating to 95 °C for 5 min followed by slow cooling to 25 °C to obtain 1 mM duplex.

Before crystallization, aliquots of the purified components were thawed on ice and buffer-exchanged into crystallization buffer (20 mM Tris·HCl, pH 8.0, 0.2 M NaCl, 5 mM DTT). $E\sigma^{70}$ was formed by adding 1.2-fold molar excess of $\Delta1.1\sigma^{70}$ to the ΔαCTD-core RNAP and incubated at room temperature for 15 min. The $E\sigma^{70}$ was then incubated with 1.2-fold molar excess of DNA (*SI Appendix*, Fig. S1*A*) for 15 min at room temperature.

The final concentration of the complex was adjusted to 40 μM. Initial crystals with CueR us-fork−38 DNA were grown via vapor diffusion at 22 °C by mixing 1 μL of sample with 1 μL of reservoir solution [0.1 M Hepes, pH 7.5, 0.2 M $MgCl_2$, 25% (wt/vol) PEG 3350, 5 mM DTT] in a 48-well hanging drop tray (Hampton Research). Further screening around this condition led to optimized crystallization conditions using CueR us-fork−35 DNA and a reservoir solution of 0.1 M Hepes, pH 6.8, 0.2 M $MgCl_2$, 7% (wt/vol) PEG 3350, 4% (vol/vol) glycerol, 4% (vol/vol) ethylene glycol, resulting in rod-shaped crystals approximately 200 × 80 × 80 μm in dimension. The crystals were transferred into reservoir solution supplemented with 10% (vol/vol) glycerol and 10% (vol/vol) ethylene glycol for cryoprotection and flash-frozen in liquid

nitrogen. For MccJ25 or Cap complexes, the crystals were incubated in reservoir solution with 100 μM peptide overnight before cryoprotection and freezing.

Data Collection, Structure Determination, and Refinement. X-ray diffraction data were collected at the Argonne National Laboratory Advanced Photon Source NE-CAT beamlines 24-ID-C and 24-ID-E. Most structural biology software was accessed through the SBGrid consortium (47). The crystals belonged to space group $P4_12_12$ (*SI Appendix*, Table S1). Many crystals were screened to find the best diffracting datasets that were combined by scaling together (*SI Appendix*, Table S1).

The structures were solved by molecular replacement by using an *Eco* $E\sigma^{70}$ model as a search model (PDB ID code 4LK1) (19). The resulting models were improved by iterative cycles of manual building with COOT (48) and refinement with PHENIX (49).

Cap Inhibition Assays. Reactions initially contained 5 pmol $E\sigma^{70}$ and 2 pmol T7A1 promoter DNA fragment in transcription buffer (50 mM Tris, pH 7.9, 100 mM KCl, 10 mM $MgCl_2$, 1 mM DTT, 50 μg/mL BSA). After 15 min at 37 °C, 1 μL of 1 mg/mL heparin was added, followed by 0, 1, 10, or 100 μM Cap. After an additional 15 min at 37 °C, RNA synthesis was initiated with the addition of 500 μM CpA and 12.5, 25, 50, or 100 μM [α-^{32}P]UTP. The final reaction volume was 40 μL. After 5 min, reactions were terminated by the addition of 40 μL stop buffer (TBE, 8 M urea, 30 mM EDTA). Products were heated for 10 min at 90 °C, resolved by urea-PAGE, and quantified by using a storage-phosphor scanner. Data were fit to models of inhibition by using SigmaPlot.

ACKNOWLEDGMENTS. We thank B. Bae, K.-A. Twist, M. Chaker-Margot, P. Olinares, and B. T. Chait for initial contributions to this project. This work is based on research conducted at the Northeastern Collaborative Access Team beamlines, which are funded by National Institute of General Medical Sciences–National Institutes of Health (NIH) Grant P41 GM103403. The Pilatus 6M detector on 24-ID-C beamline is funded by NIH-Office of Research Infrastructure Programs High-End Instruments Grant S10 RR029205. This research used resources of the Advanced Photon Source, a US Department of Energy (DOE) Office of Science User Facility operated for the DOE Office of Science by Argonne National Laboratory under ContractDE-AC02-06CH11357. The use of The Rockefeller University Structural Biology Resource Center was made possible by NIH/National Center for Research Resources Grant 1S10RR027037. This work was supported by NIH Grants R01 GM107036 (to A.J.L.) and R35 GM118130 (to S.A.D.).

1. Maksimov MO, Pelczer I, Link AJ (2012) Precursor-centric genome-mining approach for lasso peptide discovery. *Proc Natl Acad Sci USA* 109:15223–15228.
2. Maksimov MO, Link AJ (2014) Prospecting genomes for lasso peptides. *J Ind Microbiol Biotechnol* 41:333–344.
3. Arnison PG, et al. (2013) Ribosomally synthesized and post-translationally modified peptide natural products: Overview and recommendations for a universal nomenclature. *Nat Prod Rep* 30:108–160.
4. Bayro MJ, et al. (2003) Structure of antibacterial peptide microcin J25: A 21-residue lariat protoknot. *J Am Chem Soc* 125:12382–12383.
5. Rosengren KJ, et al. (2003) Microcin J25 has a threaded sidechain-to-backbone ring structure and not a head-to-tail cyclized backbone. *J Am Chem Soc* 125:12464–12474.
6. Wilson K-A, et al. (2003) Structure of microcin J25, a peptide inhibitor of bacterial RNA polymerase, is a lassoed tail. *J Am Chem Soc* 125:12475–12483.
7. Delgado MA, Rintoul MR, Farías RN, Salomón RA (2001) Escherichia coli RNA polymerase is the target of the cyclopeptide antibiotic microcin J25. *J Bacteriol* 183: 4543–4550.
8. Yuzenkova J, et al. (2002) Mutations of bacterial RNA polymerase leading to resistance to microcin j25. *J Biol Chem* 277:50867–50875.
9. Kuznedelov K, et al. (2011) The antibacterial threaded-lasso peptide capistruin inhibits bacterial RNA polymerase. *J Mol Biol* 412:842–848.
10. Salomón RA, Farías RN (1992) Microcin 25, a novel antimicrobial peptide produced by Escherichia coli. *J Bacteriol* 174:7428–7435.
11. Solbiati JO, et al. (1999) Sequence analysis of the four plasmid genes required to produce the circular peptide antibiotic microcin J25. *J Bacteriol* 181:2659–2662.
12. Adelman K, et al. (2004) Molecular mechanism of transcription inhibition by peptide antibiotic microcin J25. *Mol Cell* 14:753–762.
13. Mukhopadhyay J, Sineva E, Knight J, Levy RM, Ebright RH (2004) Antibacterial peptide microcin J25 inhibits transcription by binding within and obstructing the RNA polymerase secondary channel. *Mol Cell* 14:739–751.
14. Knappe TA, et al. (2008) Isolation and structural characterization of capistruin, a lasso peptide predicted from the genome sequence of Burkholderia thailandensis E264. *J Am Chem Soc* 130:11446–11454.
15. Metelev M, et al. (2017) Acinetodin and klebsidin, RNA polymerase targeting lasso peptides produced by human isolates of Acinetobacter gyllenbergii and Klebsiella pneumoniae. *ACS Chem Biol* 12:814–824.
16. Knappe TA, et al. (2011) Introducing lasso peptides as molecular scaffolds for drug design: Engineering of an integrin antagonist. *Angew Chem Int Ed Engl* 50: 8714–8717.
17. Pan SJ, Link AJ (2011) Sequence diversity in the lasso peptide framework: Discovery of functional microcin J25 variants with multiple amino acid substitutions. *J Am Chem Soc* 133:5016–5023.
18. Zuo Y, Wang Y, Steitz TA (2013) The mechanism of E. coli RNA polymerase regulation by ppGpp is suggested by the structure of their complex. *Mol Cell* 50:430–436.
19. Bae B, et al. (2013) Phage T7 Gp2 inhibition of Escherichia coli RNA polymerase involves misappropriation of σ70 domain 1.1. *Proc Natl Acad Sci USA* 110:19772–19777.
20. Murakami KS (2013) X-ray crystal structure of Escherichia coli RNA polymerase σ^{70} holoenzyme. *J Biol Chem* 288:9126–9134.
21. Outten FW, Outten CE, Hale J, O'Halloran TV (2000) Transcriptional activation of an Escherichia coli copper efflux regulon by the chromosomal MerR homologue, cueR. *J Biol Chem* 275:31024–31029.
22. Murakami KS, Masuda S, Campbell EA, Muzzin O, Darst SA (2002) Structural basis of transcription initiation: An RNA polymerase holoenzyme-DNA complex. *Science* 296: 1285–1290.
23. Bae B, Feklistov A, Lass-Napiorkowska A, Landick R, Darst SA (2015) Structure of a bacterial RNA polymerase holoenzyme open promoter complex. *eLife* 4:e08504.
24. Hubin EA, et al. (2017) Structure and function of the mycobacterial transcription initiation complex with the essential regulator RbpA. *eLife* 6:e22520.
25. Piscotta FJ, Tharp JM, Liu WR, Link AJ (2015) Expanding the chemical diversity of lasso peptide MccJ25 with genetically encoded noncanonical amino acids. *Chem Commun (Camb)* 51:409–412.
26. Mathavan I, et al. (2014) Structural basis for hijacking siderophore receptors by antimicrobial lasso peptides. *Nat Chem Biol* 10:340–342.
27. Krissinel E, Henrick K (2007) Inference of macromolecular assemblies from crystalline state. *J Mol Biol* 372:774–797.
28. Lane WJ, Darst SA (2010) Molecular evolution of multisubunit RNA polymerases: Structural analysis. *J Mol Biol* 395:686–704.
29. Miropolskaya N, Artsimovitch I, Klimašauskas S, Nikiforov V, Kulbachinskiy A (2009) Allosteric control of catalysis by the F loop of RNA polymerase. *Proc Natl Acad Sci USA* 106:18942–18947.
30. Pavlova O, Mukhopadhyay J, Sineva E, Ebright RH, Severinov K (2008) Systematic structure-activity analysis of microcin J25. *J Biol Chem* 283:25589–25595.
31. Vincent PA, Bellomio A, de Arcuri BF, Farías RN, Morero RD (2005) MccJ25 C-terminal is involved in RNA-polymerase inhibition but not in respiration inhibition. *Biochem Biophys Res Commun* 331:549–551.
32. Zhang G, et al. (1999) Crystal structure of Thermus aquaticus core RNA polymerase at 3.3 A resolution. *Cell* 98:811–824.
33. Batada NN, Westover KD, Bushnell DA, Levitt M, Kornberg RD (2004) Diffusion of nucleoside triphosphates and role of the entry site to the RNA polymerase II active center. *Proc Natl Acad Sci USA* 101:17361–17364.
34. Malinen AM, et al. (2012) Active site opening and closure control translocation of multisubunit RNA polymerase. *Nucleic Acids Res* 40:7442–7451.
35. Vassylyev DG, et al. (2007) Structural basis for substrate loading in bacterial RNA polymerase. *Nature* 448:163–168.
36. Wang D, Bushnell DA, Westover KD, Kaplan CD, Kornberg RD (2006) Structural basis of transcription: Role of the trigger loop in substrate specificity and catalysis. *Cell* 127: 941–954.
37. Windgassen TA, et al. (2014) Trigger-helix folding pathway and SI3 mediate catalysis and hairpin-stabilized pausing by Escherichia coli RNA polymerase. *Nucleic Acids Res* 42:12707–12721.
38. Segel IH (1975) *Enzyme Kinetics* (Wiley, New York).
39. Basu RS, et al. (2014) Structural basis of transcription initiation by bacterial RNA polymerase holoenzyme. *J Biol Chem* 289:24549–24559.
40. Degen D, et al. (2014) Transcription inhibition by the depsipeptide antibiotic salinamide A. *eLife* 3:e02451.
41. Kaplan CD, Larsson K-M, Kornberg RD (2008) The RNA polymerase II trigger loop functions in substrate selection and is directly targeted by α-amanitin. *Mol Cell* 30: 547–556.
42. Mishanina TV, Palo MZ, Nayak D, Mooney RA, Landick R (2017) Trigger loop of RNA polymerase is a positional, not acid-base, catalyst for both transcription and proofreading. *Proc Natl Acad Sci USA* 114:E5103–E5112.
43. Sassone-Corsi M, et al. (2016) Microcins mediate competition among Enterobacteriaceae in the inflamed gut. *Nature* 540:280–283.
44. Twist K-A, et al. (2011) A novel method for the production of in vivo-assembled, recombinant Escherichia coli RNA polymerase lacking the α C-terminal domain. *Protein Sci* 20:986–995.
45. Pan SJ, Cheung WL, Link AJ (2010) Engineered gene clusters for the production of the antimicrobial peptide microcin J25. *Protein Expr Purif* 71:200–206.
46. Pan SJ, Rajniak J, Maksimov MO, Link AJ (2012) The role of a conserved threonine residue in the leader peptide of lasso peptide precursors. *Chem Commun (Camb)* 48: 1880–1882.
47. Morin A, et al. (2013) Collaboration gets the most out of software. *eLife* 2:e01456.
48. Emsley P, Cowtan K (2004) Coot: Model-building tools for molecular graphics. *Acta Crystallogr D Biol Crystallogr* 60:2126–2132.
49. Adams PD, et al. (2010) PHENIX: A comprehensive Python-based system for macromolecular structure solution. *Acta Crystallogr D Biol Crystallogr* 66:213–221.
50. Zuo Y, Steitz TA (2015) Crystal structures of the E. coli transcription initiation complexes with a complete bubble. *Mol Cell* 58:534–540.
51. Lane WJ, Darst SA (2010) Molecular evolution of multisubunit RNA polymerases: Sequence analysis. *J Mol Biol* 395:671–685.